buildings

MDPI

Article

Buckling and Mechanical Behavior of Single Through-Type and Plate-Reinforced X-Shaped Concrete-Filled Steel Tubular Columns

Xufeng Wang [1], Yongfei Zhang [1], Jiangwen Wu [2], Zhengchen Ge [2,*], Xiuyuan Chen [2], Yongkai Yuan [2] and Dunfu Zhang [2,*]

[1] Shandong Electric Power Engineering Consulting Institute Corporation Limited, Jinan 250013, China
[2] School of Civil Engineering, Shandong University, Jinan 250061, China
* Correspondence: gezhengchen@mail.sdu.edu.cn (Z.G.); zhangdf@sdu.edu.cn (D.Z.); Tel.: +86-1558-9879-315 (Z.G.)

Abstract

The axial resistance and out-of-plane buckling of concrete-filled steel tubular (CFST) X-columns depend in part on the configuration of their crossing. This study compared two CFST X-column specimens, one single through-type (ST) and one plate-reinforced (PR), to assess how crossing detail relates to axial response and bending distribution. The PR configuration incorporated an intermediate plate at the crossing, while nominal tube dimensions, member lengths, branch angle, and infill were matched between configurations. Axial compression tests provided load–actuator-travel histories, while three-point post-test lateral measurements characterized residual bending around the crossing. Finite element models compared the first out-of-plane modes and stress distributions around the crossing. The PR specimen reached a 34.9% higher peak load and carried more load across the shared pre-peak displacement range. Both specimens developed overall out-of-plane buckling, while the PR specimen showed a steeper peak-normalized post-peak load decline. Post-test bending was most prominent near the ST crossing but in the adjacent lower tube for PR; joint-center chord deviations were 24.5 and 16.5 mm, respectively. Numerical modes and stress contours showed a corresponding redistribution of deformation and stress around the reinforced crossing. These findings link X-joint detailing to axial resistance and the location of out-of-plane bending, providing evidence for assessing CFST X-column configurations.

Keywords: buckling; X-shaped concrete-filled steel tubular column; single through-type (ST); plate-reinforced (PR); finite element analysis

Check for updates

Academic Editor: Vipul Patel

Received: 14 October 2026
Revised: 13 November 2026
Accepted: 16 November 2026
Published: 17 November 2026

Copyright: © 2026 by the authors. Licensee MDPI, Basel, Switzerland. This article is an open access article distributed under the terms and conditions of the Creative Commons Attribution (CC BY) license.

1. Introduction

Concrete-filled steel tubular (CFST) members resist compression through the combined action of the steel tube and its infill. The tube confines the core, while the core supports the tube wall against inward deformation [1–3]. In an X-column, two inclined CFST members meet at a welded crossing. This region connects the adjoining branches and provides restraint that is absent from an isolated straight member. Even when the tubes and infill on either side of the crossing are nominally identical, a change in the joint detail may affect the axial response of the complete assembly and the distribution of bending along its branches. Axial and eccentric loading studies of straight CFST columns have established the effects of section geometry, slenderness, and load eccentricity on strength and deformation [4–9]. Related studies have examined flexural buckling and nonlinear response in steel

and composite columns [10–12]. These findings help explain the behavior of the inclined portions of an X-column, but they do not fully describe the restraint introduced where the two members intersect.

The distinction becomes important as lateral deformation develops. Local tube buckling may accompany overall bending, and studies of CFST and other thin-walled columns have examined the influence of section shape and geometric imperfections on this interaction [13–17]. Experimental and numerical work on infilled stub columns has also considered different tube materials, concrete cores, and combinations of compression and bending [18–25]. Much of this evidence concerns members whose section remains broadly consistent along the tested length. An X-column has an additional geometric discontinuity at its crossing, making the location of bending relative to the joint and adjoining tube segments relevant to its response. Changes in member section provide one means of modifying compression behavior: studies of double-skin, L-shaped, octagonal, and slotted CFST columns show the effects of section geometry and stiffening details [26–30]. Reinforcing only the crossing differs from modifying the member along its length. Its influence must be examined in the connected assembly.

Research specifically on CFST X-columns has begun to address the role of the crossing. Chen et al. [31] studied the axial stability of slender X-columns and examined the influence of geometry on global buckling. A subsequent experimental and theoretical study compared through-type and reinforced joints [32]. The reinforced detail combined a connection plate with a liner tube, circumferential stiffening plates, and ribs; numerical analyses also examined the roles of the reinforcing components. Further work related X-column stability to variation in flexural rigidity along the assembly [33]. These studies establish the importance of the joint region, while leaving open how an intermediate plate alone changes the response when the nominal tube dimensions, infill, branch angle, and member lengths are kept the same. Reviews and axial tests of conventional CFST members document the effects of tube geometry, wall thickness, and steel–infill interaction on compression behavior [34–37]. Tests and numerical analyses of columns with longitudinal stiffeners show that stiffening can delay local tube buckling and change the load–deformation response [38,39]. More recent numerical studies have examined internal, external, and combined stiffening in UHPC-filled steel tubular columns under concentric and eccentric compression [4], and the slenderness-dependent buckling behaviour of concrete-filled double-skin stiffened columns [10]. These member-level studies provide context for examining how a plate localized at an X-joint changes restraint and bending distribution between the crossing and adjoining tubes.

Connection studies provide a closer point of reference. Axial tests of planar intersecting CFST connections have documented the behavior of tubes joined at a crossing [40]. Comparisons of CFST arch-joint forms under compression and bending have likewise shown that joint configuration affects the load-carrying behavior [41]. Analytical work has shown that compliance at the steel–concrete interface can affect the buckling of slender circular CFST columns [42]. Research on CFST load transfer describes the interaction between tube and core near regions where forces enter the composite section [43], while tests of welded fin-plate connections examine that process at a local connection [44]. Although these details and loading arrangements differ from an axially compressed X-column, they indicate why the joint should be assessed through more than ultimate load. Comparing complete load–end-shortening histories shows when two configurations begin to differ, how much load they carry at the same shortening, and how they respond beyond the peak. Measurements and analyses around the crossing can then show whether a change in joint detail is accompanied by a change in the distribution of out-of-plane bending. ANSYS 2022 has also been used to investigate CFST members and tubular joints. Gupta et al. [45] developed a nonlinear finite element model for axially loaded circular CFST columns and

compared the predicted load–deformation curves and collapse modes with experiments. Diao et al. [46] combined experiments with ANSYS models to investigate stress concentration factors in concrete-filled square tubular X-joints under brace axial tension, examining the effects of concrete infill and joint geometry.

Previous investigations have examined combined reinforcement arrangements and the stability behaviour of CFST X-columns. The influence of a single intermediate plate on axial response and on the distribution of out-of-plane bending between the crossing and adjoining tubes requires further clarification. To address this issue, the present study compares a single through-type (ST) configuration with a plate-reinforced (PR) configuration, with matching nominal tube dimensions, infill, member lengths, and branch angle. Axial compression tests compare peak resistance and peak-normalized post-peak load retention, while post-test lateral measurements characterize residual bending around the crossing. Numerical mode shapes and joint-region stress distributions provide a qualitative basis for interpreting the observed differences. These comparisons provide evidence on how reinforcement by a single intermediate plate relates to axial resistance, post-peak response, and the location of dominant residual bending.

2. Experimental Apparatus and Specimen Preparation

2.1. Specimens and Materials

The test program comprised two CFST X-shaped column specimens representing two joint configurations: a single through-type specimen (ST) and a plate-reinforced (PR) specimen incorporating an intermediate stiffening plate. One specimen was tested for each configuration. The specimens were designed with reference to CFST X-shaped columns used in ultra-large indirect air-cooled towers. Figure 1 illustrates the joint configurations and principal dimensions of the two specimens. The ST configuration has a welded tube intersection without an intermediate stiffening plate, whereas the PR configuration incorporates an intermediate plate welded at the crossing.

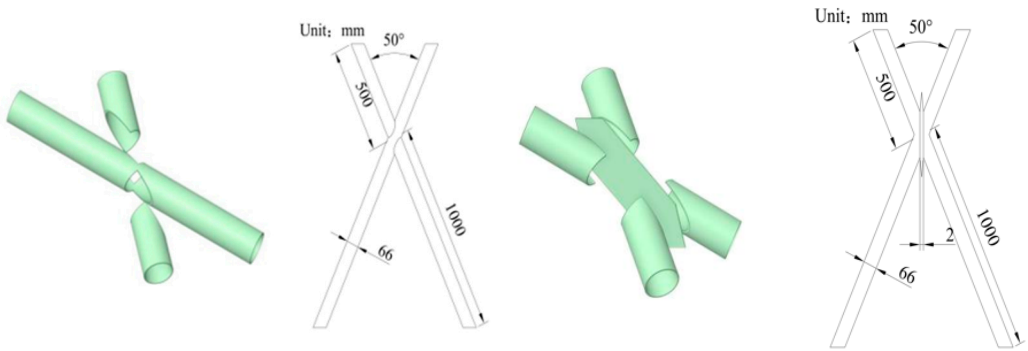

Figure 1. Geometry and dimensions of the specimens: (**a**) a single through-type specimen; (**b**) plate-reinforced specimen.

Both specimens used circular steel tubes with an outer diameter D of 66 mm and a wall thickness t of 2 mm, corresponding to D/t = 33. The upper and lower column lengths were 500 and 1000 mm, respectively, and the branch angle was 50°. The principal dimensions are shown in Figure 1 and summarized in Table 1.

Both specimens were fabricated from Q355 seamless steel tubes. “Q” denotes yield strength, and “355” indicates the nominal yield-strength grade of 355 MPa. The tubes were cut by CNC, fitted to the X-shaped geometry, and joined by gas tungsten arc welding (Figure 2a–c). The plate-reinforced specimen additionally incorporated an intermediate

plate welded at the crossing (Figure 2d). The plate measured 300 mm in length, 90 mm in width, and 2 mm in thickness, matching the tube wall thickness. The single through-type specimen had no intermediate plate.

Table 1. Geometry and infill specification of the two tested X-columns.

Specimen No.	Upper Column Length (mm)	Lower Column Length (mm)	Node Angle (°)	Core Filling Material
a single through-type X-column	500	1000	50	Non-shrinkage grout, nominal strength ~45 MPa
reinforced-type X-column	500	1000	50	Non-shrinkage grout, nominal strength ~45 MPa

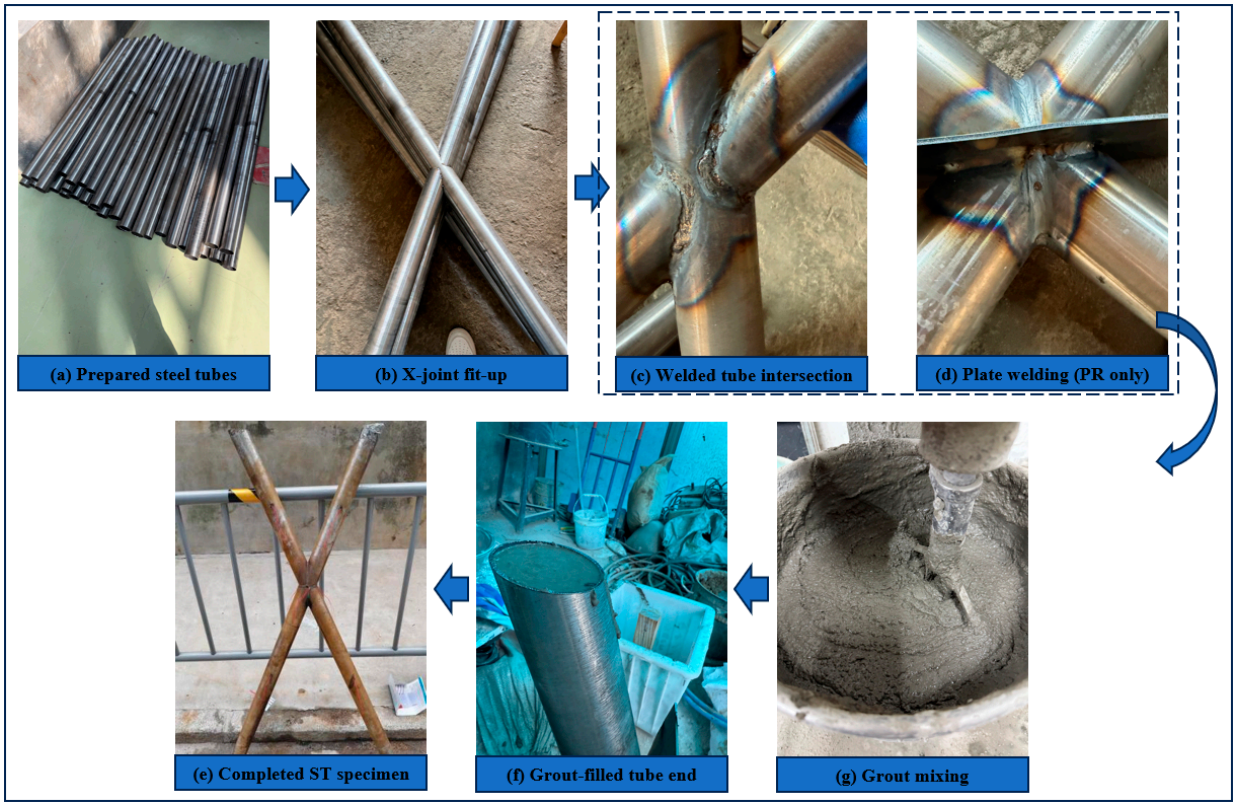

Figure 2. Selected stages of CFST X-column fabrication.

After welding and cooling, the weld surfaces were visually inspected. For grouting, both tube assemblies were positioned vertically, with the lower tube openings sealed. In the PR specimen, the intermediate stiffening plate divided the internal cavity into two regions, each connected to a separate upper opening through which grout was introduced. Both specimens were filled with high-strength non-shrinkage grout with a nominal compressive strength of approximately 45 MPa (Figure 2f,g). During filling, the grout was vibrated, the tube walls were tapped, and the specimens were moved up and down to promote consolidation and facilitate the escape of entrapped air through the open upper ends.

After the grout had hardened and before loading, the filling condition was assessed qualitatively by visual inspection and tapping of the tube walls. Both specimens were cured indoors for 28 days, and their loading ends were ground flat before testing. Figure 2e shows the completed ST specimen.

2.2. Test Setup and Loading Protocol

The axial compression tests were conducted in a reaction frame using a hydraulic jack (Shandong University, Jinan, China). The tube ends were placed in direct bearing contact with the upper and lower loading plates, with end restraint provided by the tube–plate contact. The lower plate remained stationary, and vertical compression was applied through the upper plate. Before loading, the specimen centre was aligned with the loading axis of the hydraulic jack to minimise unintended load eccentricity. Both specimens were tested using the same support and alignment arrangement. The loading plates were 1.6 m long, 0.5 m wide, and 0.2 m thick. Figure 3 shows the reaction frame, hydraulic loading device, and PR specimen positioned between the loading plates.



(**a**) (**b**) (**c**)

Figure 3. Axial-compression test setup: (**a**) reaction frame; (**b**) hydraulic loading device and upper loading plate; (**c**) plate-reinforced specimen positioned between the loading plates.

In a structural assembly, connections to adjacent members can transfer horizontal reactions and restrain in-plane movement of the tube ends. The degree of restraint depends on the connection details and the stiffness of the adjoining structure. This restraint can affect load transfer through the crossing. The tests therefore compare the ST and PR configurations under the same direct-bearing support arrangement.

Before formal loading, each specimen was preloaded to 20% of its estimated ultimate load to check the gauges, displacement transducers, and loading equipment; this preload was then removed. The ultimate load used as a reference for prescribing the loading stages was estimated from the material properties of the steel tubes and the cementitious infill. Loading proceeded to 60% of the estimated ultimate load in increments of 10% of that estimate, with each level held for 2 min. From 60% to 80%, increments were reduced to 5% and the data-acquisition frequency was increased. Beyond 80%, slow continuous loading continued until pronounced lateral deformation or a substantial load decrease occurred. Peak load and final deformation were recorded.

The displacement signal used in the response analysis was the actuator travel recorded by the hydraulic loading device. The displacement reading was zeroed before preloading. The recorded actuator travel provided the displacement coordinate for the experimental load–displacement curves.

3. Experimental Results and Analysis

This section examines the influence of the intermediate stiffening plate on the ultimate load-bearing capacity and buckling behaviour of the X-shaped specimens. The peak loads obtained from the recorded load–displacement curves are compared between the ST and PR specimens to assess the difference in ultimate capacity. Specimen photographs comple-

ment these measurements by showing the observed buckling patterns and the locations of concentrated bending and damage. Together, these results characterise the capacity and failure behaviour of the two joint configurations.

3.1. Axial Load–Shortening Response and Capacity

Response quantities at prescribed load or axial displacement levels were obtained by linear interpolation of the recorded load–displacement curves. For comparisons at a prescribed load, the displacement was taken from the ascending branch; post-peak quantities were extracted from the descending branch.

The cumulative external work $W(\delta)$ up to a target actuator travel δ was calculated from the recorded axial load–actuator-travel history using Equation (1).

$$W(\delta) = \int_0^{\delta} P(u)\mathrm{d}u \tag{1}$$

Here, u is the recorded actuator travel, and $P(u)$ is the corresponding axial load. For two consecutive records (ui, Pi) and $(ui + 1, Pi + 1)$, the work increment was calculated using the trapezoidal rule.

$$\Delta W_i = \frac{P_i + P_{i+1}}{2}(u_{i+1} - u_i).$$

When the target travel δ fell between u_i and u_{i+1}, the load $P(\delta)$ was obtained by linear interpolation. The final partial trapezoid extended from u_i to δ, giving

$$\Delta W_\delta = \frac{P_i + P(\delta)}{2}(\delta - u_i).$$

The cumulative work was obtained by summing the contributions from the complete intervals and, where applicable, the final partial interval. With load in kN and actuator travel in mm, the sum was converted to kJ using 1 kN·mm = 0.001 kJ.

Figure 4 presents the axial load–shortening responses measured between the two specimen ends. Each response has an ascending branch, a maximum, and a descending branch. The specimens separated substantially in shortening at low load: at 50 kN, the single through-type specimen had shortened by 12.01 mm and the plate-reinforced specimen by 5.51 mm. Their ascending branches then had similar secant slopes over the shared 50–150 and 200–300 kN intervals, before the reinforced specimen continued to a higher peak load.

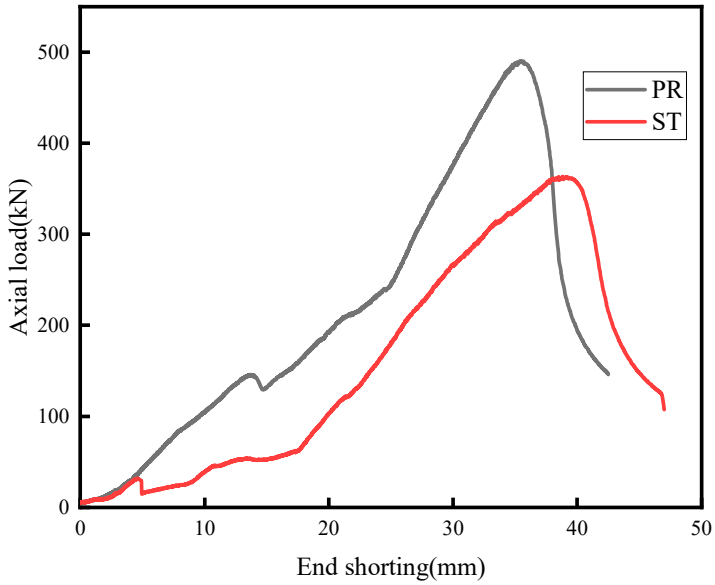

Figure 4. Experimental axial load–end shortening curves of the single through-type and plate-reinforced CFST X-columns.

To compare the responses at the same deformation level, the loads at an axial shortening of 30 mm were extracted from the original records. The single through-type and plate-reinforced specimens carried 266.73 and 376.24 kN, respectively, giving a 41.1% difference at the same shortening. Conversely, at the common load of 300 kN, the corresponding shortenings were 32.54 and 26.96 mm. The reinforced specimen therefore required 5.58 mm less axial shortening to sustain this load.

The shortening difference between the specimens was already 6.50 mm at 50 kN: 12.01 mm for the single through-type specimen and 5.51 mm for the plate-reinforced specimen. It remained 5.58 mm at 300 kN. To characterize the subsequent ascending response, secant slopes were calculated over two shared load intervals as $K_{(P_1-P_2)} = \frac{P_2-P_1}{\delta(P_2)-\delta(P_1)}$. The slopes over 50–150 kN were 8.82 and 9.01 kN/mm for the single through-type and plate-reinforced specimens; those over 200–300 kN were 15.21 and 15.52 kN/mm. Thus, much of the total-shortening separation developed at the beginning of loading, while the two specimens had similar secant slopes over these later common load intervals. The reinforced specimen then continued to a substantially higher peak load.

Table 2 summarizes the principal axial-response values. The plate-reinforced specimen reached 490.37 kN at 35.36 mm, whereas the single through-type specimen reached 363.40 kN at 38.83 mm. At the common shortening of 30 mm, the reinforced specimen carried 376.24 kN versus 266.73 kN; at the common load of 300 kN on the ascending branch, it shortened by 26.96 mm versus 32.54 mm. These comparisons show a higher attained load and lower shortening at matched pre-peak states for the tested reinforced specimen.

Table 2. Key experimental axial-response values of the two specimens.

Quantity	Single Through-Type	Plate-Reinforced	PR vs. ST (%)
Peak load, Pmax (kN)	363.40	490.37	+34.9%
Shortening at peak, δmax (mm)	38.83	35.36	−8.9%
Load at δ = 30 mm (kN)	266.73	376.24	+41.1%
Ascending-branch shortening at P = 300 kN (mm)	32.54	26.96	−17.1%

Figure 5a compares the loads carried at equal specimen-end shortenings. The plate-reinforced specimen carried 66.18, 89.12, and 109.51 kN more at 10, 20, and 30 mm, respectively (Table 3). Figure 5b shows cumulative external work; at 30 mm it was 4.575 kJ for the plate-reinforced specimen and 2.605 kJ for the single through-type specimen.

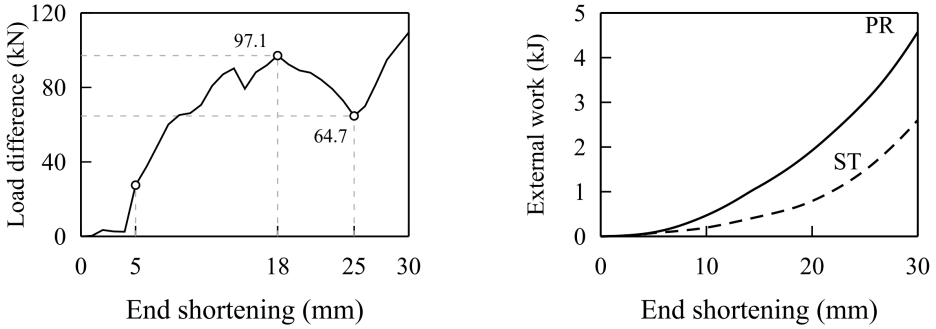

(**a**) load difference P_PR − P_ST (**b**) cumulative external work.

Figure 5. Derived experimental response at common specimen-end shortening. (**a**) load difference P_PR − P_ST; (**b**) cumulative external work. ST, single through-type; PR, plate-reinforced.

Figure 6 and Table 4 compare the descending branches using additional shortening beyond each specimen's own peak. At 2 mm beyond the peak, the retained load fractions were 90.6% for the single through-type specimen and 86.6% for the plate-reinforced specimen. At 5 mm, the absolute loads were 170.45 and 184.28 kN, respectively, corresponding

to 46.9% and 37.6% of their own peak loads. The reinforced specimen retained a slightly higher absolute load at this offset, while its peak-normalized load was lower.

Table 3. Experimental load and cumulative external work at common specimen-end shortenings. ST, single through-type; PR, plate-reinforced.

δ (mm)	P_ST (kN)	P_PR (kN)	ΔP (kN)	W_ST (kJ)	W_PR (kJ)
5	14.66	42.18	27.52	0.076	0.091
10	38.55	104.73	66.18	0.196	0.470
15	53.05	132.31	79.26	0.444	1.117
20	102.34	191.46	89.12	0.791	1.922
25	179.51	244.19	64.68	1.481	3.015
30	266.73	376.24	109.51	2.605	4.575

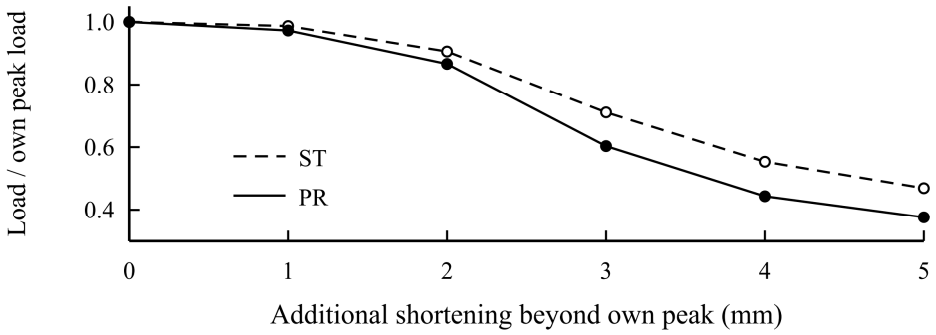

Figure 6. Peak-normalized experimental descending-branch response.

Table 4. Experimental descending-branch loads at equal additional shortenings beyond each specimen's own peak. ST, single through-type; PR, plate-reinforced.

Δδ (mm)	P_ST (kN)	P_PR (kN)	ST/Pmax (%)	PR/Pmax (%)
0	363.40	490.37	100.0	100.0
1	358.70	477.06	98.7	97.3
2	329.25	424.85	90.6	86.6
3	258.39	295.81	71.1	60.3
4	201.08	217.39	55.3	44.3
5	170.45	184.28	46.9	37.6

3.2. Failure Modes and Curvature

Both specimens exhibited overall out-of-plane buckling, with lateral deformation perpendicular to the initial plane of the X-shaped assembly. Figure 7 shows their post-test configurations and enlarged views of the dominant bending regions. In the ST specimen, pronounced bending was concentrated near the crossing (Figure 7a). In the PR specimen, the dominant bend was located in the main-tube segment below the reinforced crossing (Figure 7b).

The different bending locations can be interpreted through the local stiffening effect of the intermediate plate. The welded plate provides additional restraint against bending at the crossing and modifies force transfer between the crossing and the adjoining tube segments. This local reinforcement can reduce the concentration of bending deformation at the crossing relative to the adjacent unstiffened tubes. In the tested PR specimen, the lower main-tube segment became the dominant bending region. The plate therefore influenced the distribution of bending deformation without changing the observed overall buckling mode.

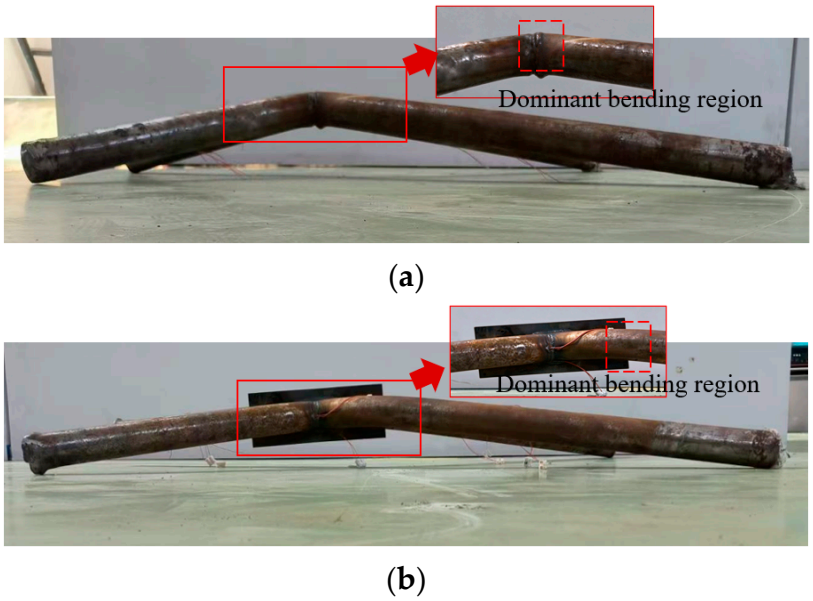

Figure 7. Post-test out-of-plane deformation and enlarged views of the dominant bending regions: (**a**) ST specimen; (**b**) PR specimen.

The joint-region stress contours in Section 4.2 provide qualitative support for this interpretation. They show a concentrated high-stress region at the ST crossing and a broader stress distribution extending into the tube below the PR crossing. The following curvature analysis provides a quantitative comparison of the post-test deformation around the crossing.

Three-point post-test measurements were used to compare residual bending around the crossing over the same longitudinal span in both specimens. The middle point was located at the crossing, and the adjacent points were positioned at longitudinal coordinate distances of 200 mm on either side. The lateral offsets were measured perpendicular to the initial plane of the X-shaped assembly. The residual curvature was estimated using a three-point finite difference.

$$|\varphi| = \frac{|y_1 - 2y_2 + y_3|}{h^2} \tag{2}$$

Here, $|\varphi|$ is the three-point finite-difference estimate of residual curvature under the small-slope approximation. The quantities y_1, y_2, and y_3 are the lateral offsets above the crossing, at the crossing, and below it, respectively. The spacing $h = 200$ mm is measured along the common reference longitudinal direction. With y and h expressed in mm, the calculated value is converted from mm^{-1} to m^{-1}. The common measurement span was adopted to compare residual bending around the crossing, where the two configurations differed in their joint detailing (Table 5).

For three equally spaced measurement positions, the deviation of the joint-center point from the straight chord joining the upper and lower points is $\Delta c = y_2 - \frac{y_1+y_3}{2}$ This quantity removes the linear component of the three-point displacement profile. Its relation to the reported finite-difference curvature is $|\varphi| = \frac{2|\Delta c|}{h^2}$, where h = 200 mm. The measurement geometry is shown in Figure 8c.

For the measured post-test shapes in Figure 8, the joint-center lateral position exceeded the straight chord joining the two adjacent positions by 24.5 mm in the single through-type specimen and 16.5 mm in the plate-reinforced specimen. The corresponding three-point finite-difference curvature estimates were 1.23 and 0.83 m^{-1}. Both quantities describe the residual shape over the same 400 mm measurement span.

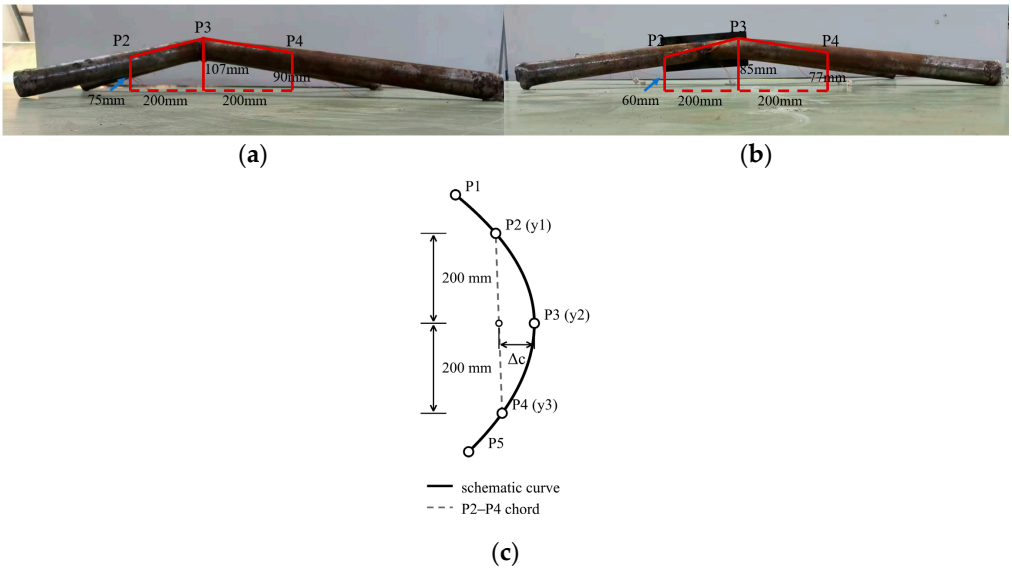

Figure 8. Post-test three-point lateral-profile measurements: (**a**) single through-type specimen; (**b**) plate-reinforced specimen; (**c**) measurement positions and definition of the joint-center chord deviation Δc (schematic).

Table 5. Measured post-test lateral displacements and joint-region curvature.

Specimen	y_1 (mm)	y_2 (mm)	y_3 (mm)	h (mm)	|Δc| (mm)	|φ| (m^{-1})
Single through-type	75	107	90	200	24.5	1.23
Plate-reinforced	60	85	77	200	16.5	0.83

The chord-deviation measure removes the linear lateral-displacement component across the three measurement positions. The reinforced specimen had a smaller local change in lateral position around the joint in its final shape; the visual post-test configuration also placed its dominant bending below the intersection (Figure 7).

4. Finite Element Analysis

4.1. Numerical Model, Mesh Response, and Comparison with the Tests

Three-dimensional finite element models were developed in ANSYS for the ST and PR configurations, with the intermediate plate and its connections included in the PR model. Both models used the same nominal material parameters, boundary conditions, and loading procedure. The Q355 steel tubes were represented by a von Mises elastoplastic model with multilinear isotropic hardening. The nominal material properties of Q355 steel were selected with reference to the relevant Chinese national standards. Young's modulus *Es* and Poisson's ratio ν_s were set to 2.06×10^5 MPa and 0.30, respectively. The infill was simulated using a confined concrete constitutive model to account for the confinement provided by the surrounding steel tube. Comparable three-dimensional nonlinear modelling approaches have recently been used for stiffened UHPC-filled steel tubular columns [4] and slender double-skin stiffened CFST columns [10]. These studies examine the composite response of steel and concrete and assess numerical predictions against experimental load–deformation behaviour, providing methodological context for the modelling and experimental comparisons adopted here.

Bonded contacts were assigned to the steel tube–infill interfaces and tube intersections to maintain displacement compatibility. Weld regions were represented by high-stiffness bonded connections to provide continuous load transfer. In both finite element models, the lower tube ends were restrained against translation in all three global directions, and axial

compression was applied by prescribing a remote displacement at the upper tube ends (Figure 9). Displacement control was used to trace the nonlinear response beyond the peak load. The steel tubes and infill were represented as three-dimensional solids to examine their stress distributions alongside the deformation of the assembly. Tetrahedral elements were selected to accommodate the curved tube surfaces and the irregular geometry at the crossing, including the plate-to-tube connections in PR. Figure 9 shows the complete model meshes together with the end boundary conditions and displacement loading. Global element sizes of 25, 15, and 10 mm were evaluated for both configurations, with peak load used as the mesh-response metric. Table 6 shows the corresponding element counts and compares the predicted peak loads with the experimental results.

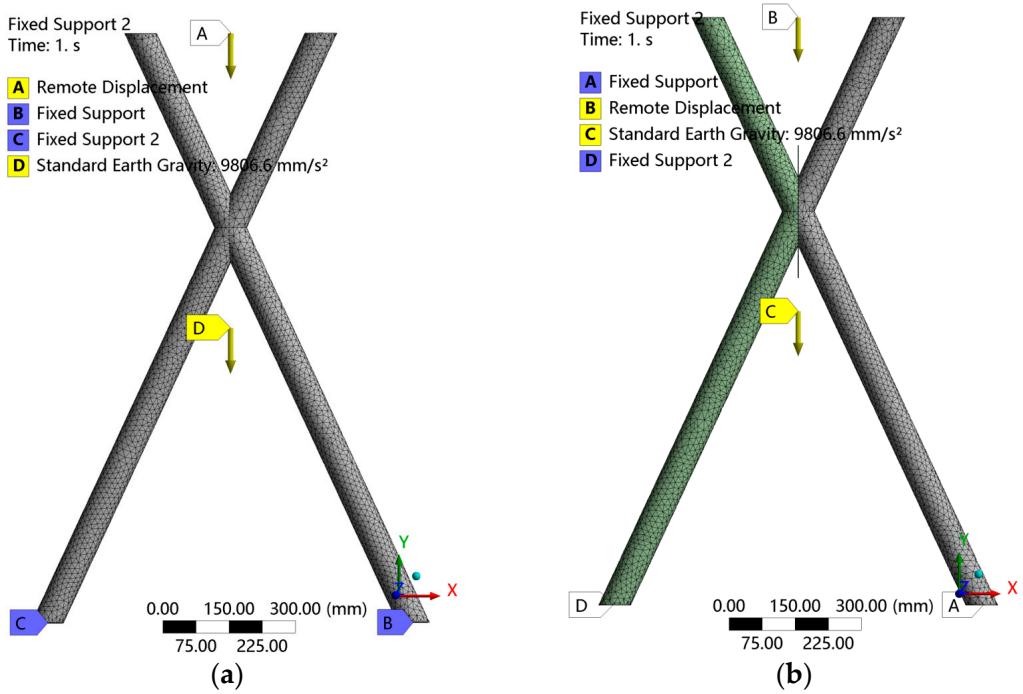

Figure 9. Finite element meshes, end boundary conditions, and displacement loading: (**a**) ST model; (**b**) PR model.

Table 6. Mesh sizes, element counts, and experimental–numerical peak-load comparisons.

Configuration	Global Mesh Size (mm)	Number of Elements	Experimental Peak Load (kN)	Numerical Peak Load (kN)	Deviation (%)
ST	25	18,427	363.40	341.34	−6.07
	15	40,926		318.80	−12.27
	10	87,799		320.69	−11.75
PR	25	18,532	490.37	360.67	−26.45
	15	41,012		346.63	−29.31
	10	84,456		330.74	−32.55

Table 6 compares the experimental peak loads with the numerical predictions for the three global mesh sizes. The deviation is calculated relative to the corresponding experimental peak load.

All three meshes underpredicted the experimental peaks. The deviations ranged from −12.27% to −6.07% for ST and from −32.55% to −26.45% for PR. Mesh refinement affected the two configurations differently: the ST peak changed non-monotonically, whereas the PR peak decreased as the mesh was refined. Finer meshes therefore did not uniformly improve agreement with the experimental peaks.

Refinement from 15 to 10 mm changed the ST and PR peaks by +0.59% and −4.58%, respectively, relative to the 15 mm results. The predicted PR/ST peak-load increases were 5.66%, 8.73%, and 3.13% for the 25, 15, and 10 mm meshes, compared with 34.94% for the experimental specimen pair. All meshes reproduced the higher PR peak, while the magnitude of the predicted PR/ST increase remained sensitive to mesh size. The difference between the experimental and numerical PR/ST increases may be associated with the representation of material response and local joint action. As bending develops, the reinforcement benefit depends on force sharing between the plate, tube walls and infill. Differences between the nominal constitutive descriptions, idealized bonded connections and the actual material and connection responses could affect the two configurations unequally. The effective end restraint may also influence how the local reinforcement contributes to the overall resistance.

The 15 mm mesh was retained as the reference discretisation for the subsequent load–shortening, deformation and stress comparisons, considering the changes in individual peak loads alongside model size. Refinement to 10 mm changed the ST and PR peaks by +0.59% and −4.58%, respectively, while increasing the element counts from 40,926 to 87,799 for ST and from 41,012 to 84,456 for PR. Table 7 presents the characteristic experimental responses and numerical predictions for these models.

Table 7. Characteristic experimental and numerical axial-response values for both joint configurations. For the final column, shortening is measured 5 mm beyond the peak of each respective curve.

Configuration	Source	Peak P (kN)	δ at Peak (mm)	P at 30 mm (kN)	δ at 300 kN (mm)	P at Peak + 5 mm (kN)
Single through-type	Test	363.40	38.83	266.73	32.54	170.45
Single through-type	FE, 15 mm	318.80	36.8	260	33.2	190
Plate-reinforced	Test	490.37	35.36	376.24	26.96	184.28
Plate-reinforced	FE, 15 mm	346.63	34.2	320	27.8	205

At a common 30 mm shortening, the 15 mm FE models carried 260 kN (single through-type) and 320 kN (plate-reinforced), 2.5% and 14.9% below the corresponding experimental loads. At a common 300 kN reaction, the FE shortenings were 33.2 and 27.8 mm, compared with 32.54 and 26.96 mm in the tests. The predicted peak shortenings were 36.8 and 34.2 mm, respectively. At 5 mm beyond each curve's own peak, the FE loads were 190 and 205 kN, equivalent to 59.6% and 59.1% of the respective FE peak loads; the corresponding experimental fractions were 46.9% and 37.6%.

4.2. Out-of-Plane Deformation and Joint-Region Stress Distribution

The numerical deformation patterns were broadly consistent with the experimental observations. Figure 10 compares the post-test photographs with the deformed shapes from the nonlinear finite element analyses in side and front views. Both configurations exhibited overall out-of-plane bending in the tests and simulations. For the ST configuration, the most pronounced bend occurred near the X-joint in both the experiment and simulation; for the PR configuration, it was more prominent in the adjoining lower main-tube segment.

The first-order buckling eigenvectors were normalised separately for the ST and PR models, with the largest displacement component of each eigenvector set to unity. Figure 11 compares the corresponding total modal deformation distributions. Both models exhibited overall out-of-plane bending, with different distributions of relative modal amplitude along the specimen height.

In the ST model, the maximum modal amplitude occurred at a height of 0.9375 m, towards the upper side of the crossing. The maximum amplitude in the lower segment was approximately 0.59 times that in the upper segment, indicating more pronounced modal movement in the upper part. In the PR model, the maximum occurred at 0.7188 m,

near the centre of the joint region, and the lower-to-upper amplitude ratio increased to approximately 1.13. The upper and lower segments therefore exhibited more comparable maximum amplitudes in the reinforced configuration.

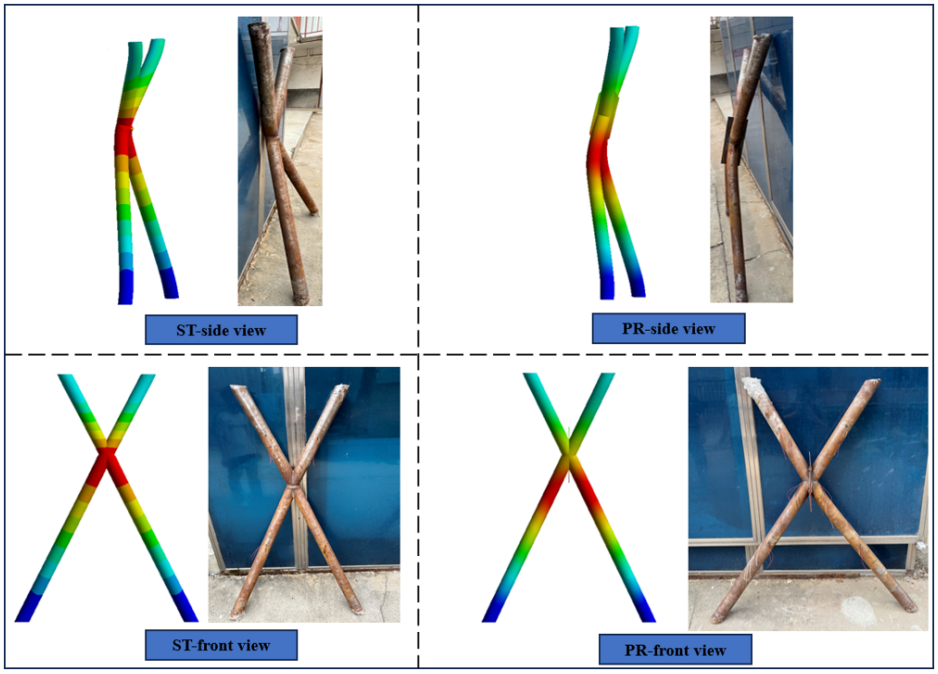

Figure 10. Comparison of experimental and numerical deformed configurations.

The shift in the modal maximum towards the crossing, together with the change in the lower-to-upper amplitude ratio, indicates that the intermediate plate modified the spatial distribution of modal deformation between the joint and the adjoining tube segments. This change is consistent with the additional local bending restraint provided by the plate at the crossing.

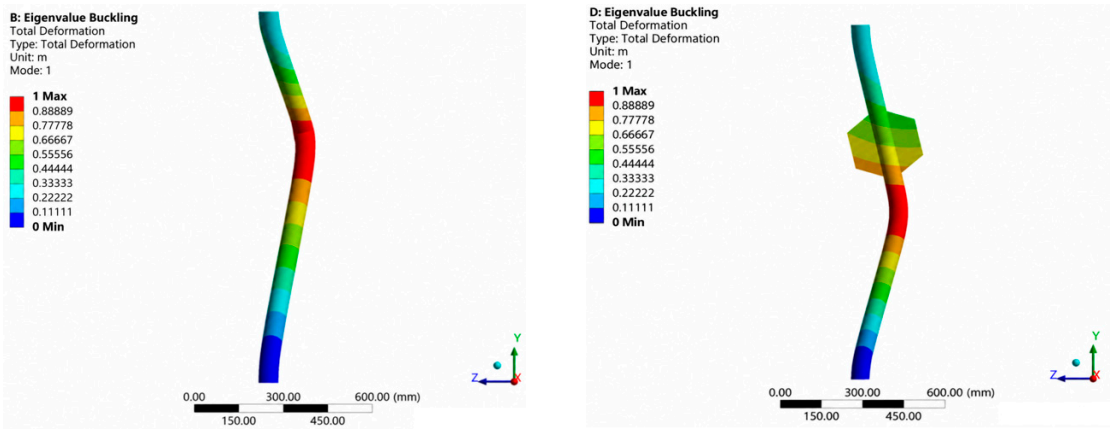

(**a**) (**b**)

Figure 11. First out-of-plane eigenmode of the CFST X-columns: (**a**) single through-type; (**b**) plate-reinforced. Modal amplitudes are normalized separately for shape comparison.

Figure 12 compares the von Mises stress distributions in the steel tubes at the respective numerical peak-load states. The maximum stresses were 494.7 MPa for the single through-type model and 477.9 MPa for the plate-reinforced model. The two values differed by only 3.4%, indicating that the principal numerical difference concerned the location and extent of the high-stress regions rather than the peak stress.

In the single through-type model, high stresses developed near the loaded and restrained ends and along the welded tube intersection. The stresses near the member ends approached 490 MPa, while those along the intersection curve were approximately 480–495 MPa. In the plate-reinforced model, high stresses also occurred near the member ends, where the values were approximately 460–478 MPa. Within the joint region, several broader high-stress zones developed in the main-tube segment below the intersection, with stresses of approximately 370–420 MPa. The intermediate stiffening plate was generally subjected to lower stresses of approximately 50–150 MPa, with localized increases near its edges. Compared with the narrow stress band in the single through-type model, the stresses in the reinforced joint were distributed over the plate edges and the adjacent main-tube region.

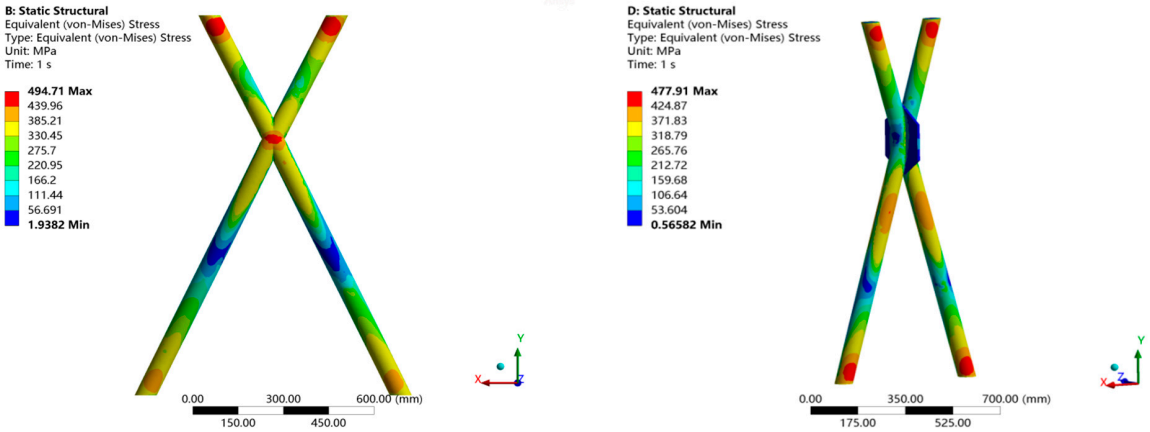

(**a**) (**b**)

Figure 12. Steel-tube von Mises stress contours: (**a**) single through-type model; (**b**) plate-reinforced model.

Figure 13 shows that the two models have similar reported maximum shear stresses, while the contours around their X-joints differ. Both plots also show elevated shear-stress bands toward the upper member ends. For comparing the joint details, the more informative feature is how the contours change at the crossing and extend into the adjoining tubes.

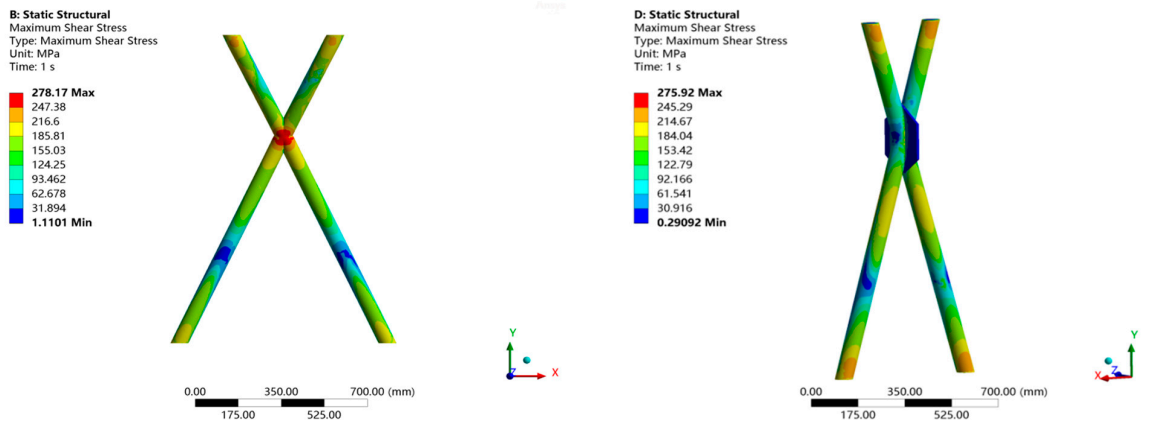

(**a**) (**b**)

Figure 13. Maximum shear stress contours of the infill material: (**a**) single through-type model; (**b**) plate-reinforced model.

In the single through-type model (Figure 13a), the highest visible contour band forms a compact red region at the intersection. Orange and yellow bands surround it, then give way to lower contour levels within a short distance along the branches. This steep change

makes the crossing the dominant interior feature of the shear-stress field. The adjoining members continue to carry shear, but their contours are less concentrated: intermediate bands extend along the lower branches and are interrupted by cooler patches farther from the joint.

The plate-reinforced model does not show a comparable red hotspot at the center of the plotted crossing (Figure 13b). Instead, warmer shear-stress bands are visible in the tube segments adjoining the connection, particularly below it. These bands extend along the lower branches before passing into cooler regions farther down the members. The upper branches also show changes near the joint, but the visible field lacks the sharp, small central concentration seen in the single through-type model.

Thus, similar maximum shear-stress values coexist with different joint-region distributions. The single through-type model has a pronounced concentration at the intersection, while the plate-reinforced plot shows more prominent shear-stress bands in the adjoining members. This central-region contrast agrees with the change in steel-stress distribution shown in Figure 12.

5. Discussion

The principal experimental effect of the intermediate plate was an increase in the load that the X-column could carry as compression progressed. At 50 kN, the two specimens already differed by 6.50 mm in end shortening. Thereafter, their secant slopes differed by only 2.2% over 50–150 kN and 2.0% over 200–300 kN. The larger peak resistance thus occurred alongside nearly unchanged secant slopes across these two shared ascending intervals. At a common 30 mm shortening, the reinforced specimen carried 109.51 kN more load, and its peak exceeded that of the single through-type specimen by 126.97 kN (34.9%). The joint detail had its clearest measured effect on the attainable load in the upper part of the response.

The same comparison separates load capacity from the work required to reach a given shortening. By 30 mm, the reinforced specimen had received 4.575 kJ of external work, compared with 2.605 kJ for the single through-type specimen, an increase of 75.6% (Figure 5b). This follows from the higher load sustained over the common shortening range. The relative advantage changed after the peak: at 5 mm of additional shortening, the reinforced specimen retained 37.6% of its own peak load, compared with 46.9% for the single through-type specimen (Figure 6). Its absolute load at that point remained slightly higher, 184.28 versus 170.45 kN. Thus, the plate increased peak resistance and pre-peak external work in this test pair, while the normalized descending branch fell more steeply.

Both specimens developed overall out-of-plane buckling, but their final bending was distributed differently around the X-joint. Across the same 400 mm measurement span, the joint-center deviation from the chord joining the upper and lower points was 24.5 mm in the single through-type specimen and 16.5 mm in the reinforced specimen, a reduction of 32.7% (Section 3.2). The corresponding finite-difference curvature estimates were 1.23 and 0.83 m^{-1}. Because the chord measure removes the straight-line component of the three-point profile, it isolates the local change in residual lateral position around the joint. The post-test photographs also show more prominent bending in the main-tube segment below the reinforced joint (Figure 7).

The numerical deformation patterns and stress contours help interpret the observed redistribution of bending around the crossing. Compared with the ST model, the PR mode placed relatively more lateral movement in the adjoining lower segment (Figure 11). In ST, high stresses were concentrated along the welded intersection. In PR, they were distributed more broadly around the plate edges and adjoining lower tube (Figure 12). The post-test profiles also showed less concentrated bending around the reinforced crossing

(Figures 7 and 14). Together, these observations indicate that local stiffening at the crossing changed the distribution of bending within the assembly while preserving the overall out-of-plane bending mode.

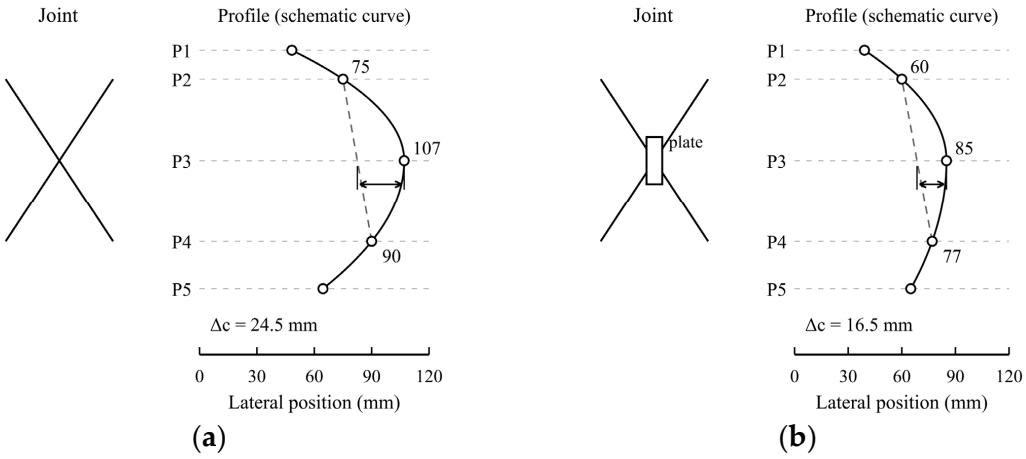

Figure 14. Joint geometry and post-test three-point out-of-plane profiles. (**a**) single through-type; (**b**) plate-reinforced.

The numerical peak-load comparison agrees with the experimental ordering but gives a smaller separation between joint details. At a 15 mm global mesh size, the reinforced model reached a peak 8.7% above the single through-type model; at 10 mm, the separation was 3.1% (Table 6). The experimental increase was 34.9%. At 30 mm shortening, the 15 mm models were 2.5% and 14.9% below the respective experimental loads; at 5 mm beyond each curve's peak, both models retained a larger fraction of peak load than the corresponding tests (Table 7). The tests establish the magnitude of the capacity difference for the specimens studied here. The numerical modes and stress contours characterize the associated changes in joint-region deformation and stress distribution.

6. Conclusions

This study compared two CFST X-column specimens with single through-type and plate-reinforced joints through axial compression tests and finite element analyses. The main conclusions are as follows.

(1) The configuration of the X-joint can influence the attainable axial resistance of CFST X-columns. In this study, PR reached 490.37 kN, compared with 363.40 kN for ST, corresponding to a 34.9% difference. At 30 mm end shortening, PR carried 41.1% more load than ST. The two specimens nevertheless showed similar secant slopes over the selected common pre-peak load intervals.

(2) The effect of joint reinforcement on peak resistance can differ from its effect on post-peak load retention. In this study, at 5 mm beyond each specimen's own peak shortening, PR and ST retained 37.6% and 46.9% of their respective peak loads. The corresponding absolute loads were 184.28 and 170.45 kN, respectively. PR therefore retained a slightly higher absolute load but a smaller fraction of its peak load.

(3) Local stiffening at the crossing can redistribute out-of-plane bending between the joint and the adjoining tube segments. In this study, both specimens exhibited overall out-of-plane buckling, with dominant residual bending near the ST crossing and in the adjoining lower tube of PR. The post-test joint-center chord deviations were 24.5 and 16.5 mm for ST and PR, respectively. Numerical mode shapes and stress contours provided qualitative support for this difference in bending distribution.

The findings provide an illustrative comparison based on a single specimen of each joint configuration under the adopted test conditions. The repeatability of the observed differences and their sensitivity to specimen-to-specimen variability remain to be established. The numerical analyses examine the tested geometry, with the mesh study assessing discretization sensitivity at this scale. Application to full-scale structural members requires further assessment of structural size effects, member slenderness, plate-to-tube proportions, and the restraint provided by adjoining structural connections.

Author Contributions: Conceptualization, X.W. and Z.G.; methodology, X.W. and Y.Z.; software, J.W.; validation, X.C.; formal analysis, X.C.; investigation, Y.Y.; resources, Z.G.; data curation, Y.Z.; writing—original draft preparation, X.W.; writing—review and editing, Z.G. and D.Z.; visualization, Z.G.; supervision, Z.G.; project administration, Y.Y.; funding acquisition, D.Z. All authors have read and agreed to the published version of the manuscript.

Funding: This research received no external funding.

Data Availability Statement: Data will be made available on request.

Conflicts of Interest: Authors Xufeng Wang and Yongfei Zhang were employed by the Shandong Electric Power Engineering Consulting Institute Corporation Limited, Jinan, China. The remaining authors declare that the research was conducted in the absence of any commercial or financial relationships that could be construed as potential conflicts of interest.

References

1. Zeghiche, J.; Chaoui, K. An experimental behaviour of concrete-filled steel tubular columns. *J. Constr. Steel Res.* **2005**, *61*, 53–66. [CrossRef]
2. Han, L.-H.; Yao, G.-H.; Zhao, X.-L. Tests and calculations for hollow structural steel (HSS) stub columns filled with self-consolidating concrete (SCC). *J. Constr. Steel Res.* **2005**, *61*, 1241–1269. [CrossRef]
3. Liang, Z.-S.; Han, L.-H. Trussed concrete-filled steel tubular hybrid structures subjected to axial compression: Performance and design calculation. *Eng. Struct.* **2024**, *302*, 117465. [CrossRef]
4. Zahra, H.G.; Mahmoud, N.; Badr, A.; Salem, F.A.; Ghannam, M. Axial compression strength of circular and square UHPC-filled stiffened steel tubular columns. *J. Constr. Steel Res.* **2025**, *227*, 109362. [CrossRef]
5. Dundu, M. Compressive strength of circular concrete filled steel tube columns. *Thin-Walled Struct.* **2012**, *56*, 62–70. [CrossRef]
6. Yu, C.-Q.; Tong, J.-Z.; Tong, G.-S. Behavior and design of slender concrete-filled wide rectangular steel tubular columns under axial compression. *Structures* **2021**, *33*, 3137–3146. [CrossRef]
7. Wang, R.; Li, X.; Zhao, H.; Wang, Y.-H.; Lam, D.; Chen, M.-T. Eccentric compression performance of round-ended CFST slender columns with different aspect ratios. *J. Constr. Steel Res.* **2023**, *211*, 108198. [CrossRef]
8. Zhang, T.; Lu, L.; Ren, Q.; Ding, J.; Wang, Q. Eccentric compressive behavior of circular steel slag concrete-filled steel tube slender columns. *Structures* **2025**, *72*, 108258. [CrossRef]
9. Shaker, F.M.F.; Daif, M.S.; Deifalla, A.F.; Ayash, N.M. Parametric Study on the Behavior of Steel Tube Columns with Infilled Concrete—An Analytical Study. *Sustainability* **2022**, *14*, 14024. [CrossRef]
10. Hassanein, M.F.; Jiang, S.-Q.; Shao, Y.-B.; Cashell, K.A. Slender concave-corner-free concrete-filled double-skin stiffened steel tubular columns for composite modular structures: Behaviour and design. *Structures* **2026**, *86*, 111376. [CrossRef]
11. Du, T.; Liu, F.; Yang, H.; Li, Y. Buckling behaviour of high-strength concrete-filled high-strength steel tubular columns after fire exposure. *Thin-Walled Struct.* **2026**, *224*, 114640. [CrossRef]
12. Ellobody, E.; Young, B. Nonlinear analysis of concrete-filled steel SHS and RHS columns. *Thin-Walled Struct.* **2006**, *44*, 919–930. [CrossRef]
13. Zhu, J.; Chen, J.; Zhang, L.; Zhang, Y.; Chan, T.-M. Numerical investigation and design recommendation for thin-walled octagonal concrete filled steel tubes. *Thin-Walled Struct.* **2023**, *188*, 110801. [CrossRef]
14. Wang, S.; Wang, W.; Xie, Z. Nonlinear cyclic behavior of steel tube in concrete-filled steel tube members including local buckling. *Thin-Walled Struct.* **2023**, *191*, 111055. [CrossRef]
15. Dubina, D.; Ungureanu, V. Local/distortional and overall interactive buckling of thin-walled cold-formed steel columns with open cross-section. *Thin-Walled Struct.* **2023**, *182*, 110172. [CrossRef]
16. Li, B.-S.; Long, Y.-L.; Yue, X.-H. Local buckling behaviour of the steel tube in elliptical CFST columns. *Structures* **2025**, *75*, 108648. [CrossRef]

17. Lin, S.; Li, J.; Yang, D.; Zhao, Y.-G. Semi-analytical model of axial load-bearing capacity of circular defective concrete-filled steel tube columns considering local buckling. *Eng. Struct.* **2026**, *346*, 121693. [CrossRef]
18. Fellah, F. Comparative Study of Calculation Models for the Fire Resistance of Hollow Steel Columns Filled with Concrete. *Period. Polytech. Civ. Eng.* **2020**, *64*, 169–187. [CrossRef]
19. Manikanta Kopuri, N.A.G.K.; Anitha Priyadharshani, S. Numerical analysis of concrete filled steel tube columns using ABAQUS. *Mater. Today Proc.* **2022**, *65*, 3476–3482. [CrossRef]
20. Zhong, Y.; Sun, Y.; Hai Tan, K.; Zhao, O. Testing, modelling and design of high strength concrete-filled high strength steel tube (HCFHST) stub columns under combined compression and bending. *Eng. Struct.* **2021**, *241*, 112334. [CrossRef]
21. Zhong, Y.; Zhao, O.; Young, B. Experimental and numerical investigations of recycled aggregate concrete-filled stainless steel tube stub columns under combined compression and bending. *Eng. Struct.* **2022**, *266*, 114502. [CrossRef]
22. Dai, P.; Yang, L.; Yun, X.; Wang, F.; Zhang, L. Experimental study of concrete-filled stainless steel tubular stub columns with circular and square cross-sections subjected to combined compression and bending. *Eng. Struct.* **2024**, *305*, 117773. [CrossRef]
23. Ma, Y.-X.; Zhao, O.; Tan, K.H. Experimental and numerical studies of concrete-encased concrete-filled steel tube stub columns under uniaxial and biaxial eccentric compression. *Eng. Struct.* **2021**, *232*, 111796. [CrossRef]
24. Han, L.-H.; Liu, W.; Yang, Y.-F. Behaviour of concrete-filled steel tubular stub columns subjected to axially local compression. *J. Constr. Steel Res.* **2008**, *64*, 377–387. [CrossRef]
25. Huang, H.; Han, L.-H.; Tao, Z.; Zhao, X.-L. Analytical behaviour of concrete-filled double skin steel tubular (CFDST) stub columns. *J. Constr. Steel Res.* **2010**, *66*, 542–555. [CrossRef]
26. Huang, H.; Wang, Y.; Zhang, L.; Chen, M.; Zhu, Y. Study on the mechanical behavior of L-shaped concrete-filled steel tubular columns under axial compression. *Struct. Concr.* **2023**, *24*, 2475–2489. [CrossRef]
27. Wei, X.; Yang, Y.; Liu, J.; Yang, W.; Chen, Y.F.; Zhang, H. Experimental and numerical study of fire performance of L-shaped concrete-filled steel tubular columns under eccentric compression. *J. Build. Eng.* **2022**, *50*, 104149. [CrossRef]
28. Ebadi Jamkhaneh, M.; Kafi, M.A. Experimental and Numerical Study of Octagonal Composite Column Subject to Various Loading. *Period. Polytech. Civ. Eng.* **2017**, *62*, 413–422. [CrossRef]
29. Rong, C.; Peng, Y.; Shi, Q.; Wang, P. Eccentric compression performance of concrete filled steel tube slotted columns: Experiment and simulation analysis. *Structures* **2025**, *74*, 108580. [CrossRef]
30. Li, S.; Liu, F.; Chan, T.-M.; Yang, H.; Young, B. Stub column behaviour of high strength steel square hollow sections with semi-circular stiffeners. *Thin-Walled Struct.* **2025**, *208*, 112687. [CrossRef]
31. Chen, D.; Zha, X.; Xu, P.; Li, W. Stability of slender concrete-filled steel tubular X-column under axial compression. *J. Constr. Steel Res.* **2021**, *185*, 106876. [CrossRef]
32. Chen, D.; Zha, X.; Xu, P.; Zhai, X. Experimental and theoretical investigation of concrete-filled steel tubular X-column under axial compression. *J. Constr. Steel Res.* **2020**, *170*, 106085. [CrossRef]
33. Chen, D.; Zha, X.; Fan, Y. Theoretical and experimental investigations on the stability performance of concrete-filled steel tubular X-column with regard to the flexural rigidity variation. *J. Build. Eng.* **2023**, *78*, 107698. [CrossRef]
34. Han, L.-H.; Li, W.; Bjorhovde, R. Developments and advanced applications of concrete-filled steel tubular (CFST) structures: Members. *J. Constr. Steel Res.* **2014**, *100*, 211–228. [CrossRef]
35. Schneider, S.P. Axially loaded concrete-filled steel tubes. *J. Struct. Eng.* **1998**, *124*, 1125–1138. [CrossRef]
36. O'Shea, M.D.; Bridge, R.Q. Design of circular thin-walled concrete filled steel tubes. *J. Struct. Eng.* **2000**, *126*, 1295–1303. [CrossRef]
37. Sakino, K.; Nakahara, H.; Morino, S.; Nishiyama, I. Behavior of centrally loaded concrete-filled steel-tube short columns. *J. Struct. Eng.* **2004**, *130*, 180–188. [CrossRef]
38. Tao, Z.; Han, L.-H.; Wang, D.-Y. Experimental behaviour of concrete-filled stiffened thin-walled steel tubular columns. *Thin-Walled Struct.* **2007**, *45*, 517–527. [CrossRef]
39. Tao, Z.; Uy, B.; Han, L.-H.; Wang, Z.-B. Analysis and design of concrete-filled stiffened thin-walled steel tubular columns under axial compression. *Thin-Walled Struct.* **2009**, *47*, 1544–1556. [CrossRef]
40. Huang, C.; Han, X.-L.; Ji, J.; Tang, J.-M. Behavior of concrete-filled steel tubular planar intersecting connections under axial compression, Part 1: Experimental study. *Eng. Struct.* **2010**, *32*, 60–68. [CrossRef]
41. Sun, H.; Lu, W.; Wang, J.; Ren, Q.; Xu, X.; Han, D.; Li, X.; Yang, H.; Wei, L.; Liu, Y. Comparative Study on Compressive and Flexural Properties of Concrete-Filled Steel Tubular Arch Joints. *Sustainability* **2022**, *14*, 8916. [CrossRef]
42. Schnabl, S.; Jelenić, G.; Planinc, I. Analytical buckling of slender circular concrete-filled steel tubular columns with compliant interfaces. *J. Constr. Steel Res.* **2015**, *115*, 252–262. [CrossRef]
43. Debnath, P.P.; Xu, F.; Chan, T.-M. Load transfer mechanism in concrete-filled steel tubular columns: Developments, challenges and opportunities. *J. Constr. Steel Res.* **2023**, *203*, 107781. [CrossRef]
44. Ning, W.; Debnath, P.P.; Chan, T.-M.; Elghazouli, A.Y. Load transfer mechanisms in welded fin plate-to-CFST column connections. *J. Struct. Eng.* **2026**, *152*, 04026050. [CrossRef]

45. Gupta, P.K.; Sarda, S.M.; Kumar, M.S. Experimental and computational study of concrete filled steel tubular columns under axial loads. *J. Constr. Steel Res.* **2007**, *63*, 182–193. [CrossRef]
46. Diao, Y.; He, S.; Wang, Y.; Tu, L. Experimental and numerical investigations on stress concentration factors of concrete filled steel tube X-joints. *Sci. Rep.* **2024**, *14*, 11415. [CrossRef] [PubMed]

Disclaimer/Publisher's Note: The statements, opinions and data contained in all publications are solely those of the individual author(s) and contributor(s) and not of MDPI and/or the editor(s). MDPI and/or the editor(s) disclaim responsibility for any injury to people or property resulting from any ideas, methods, instructions or products referred to in the content.